# Geometric Scaling of Applied-Field Magnetoplasmadynamic Thrusters

Roger M. Myers*

*Sverdrup Technology, Inc., Brook Park, Ohio 44142*

Eight magnetoplasmadynamic thruster configurations were tested with argon propellant at power levels between 20 – 130 kW to study the effects of geometry and applied magnetic field strength on thruster performance. The discharge voltage, thrust efficiency, and specific impulse increased monotonically with increasing applied-field strength for all geometries. The highest measured performance was 23% thrust efficiency at 2300-s specific impulse at a power of 113 kW. Both cathode and anode radii fundamentally influenced the efficiency-specific impulse relationship, whereas their lengths influenced only the magnitude of the applied magnetic field required to reach a given performance level. At a given specific impulse, large electrode radii resulted in lower efficiencies, although the rate at which efficiency increased with applied-field strength was higher with larger anode radii. Anode power deposition was the largest efficiency loss, and represented between 50 – 80% of the input power. The fraction of the input power deposited into the anode decreased with increasing applied-field strength and anode radius.

## Nomenclature

$B_z$ = magnetic field strength, T
$D_e$ = electron diffusion coefficient
$E$ = electric field, V/m
$e$ = electric charge, C
$I_{sp}$ = specific impulse, s
$J_d$ = discharge current, A
$k_1, k_2, k_3, k_4$ = proportionality constants
$L_a, L_c$ = anode and cathode lengths, cm
$l_n(\Lambda)$ = coulomb logarithm
$\dot{m}$ = mass flow rate, g/s
$m_e$ = electron mass, kg
$n_e$ = electron density, m$^{-3}$
$R_a, R_c$ = anode and cathode radii, cm
$r_c$ = electron cyclotron radius, m
$T$ = thrust, N
$T_e$ = electron temperature, eV
$V_{an}$ = effective anode fall, V
$V_d$ = discharge voltage, V
$\eta$ = thruster efficiency
$\lambda_D$ = Debye length, cm
$\mu_e$ = electron mobility
$\mu_0$ = permeability of free space
$\nu_{e\text{-}i}$ = electron-ion collision frequency, s$^{-1}$
$\phi$ = anode work function, V
$\omega_{ce}$ = electron cyclotron frequency, s$^{-1}$

## Introduction

**M**AGNETOPLASMADYNAMIC (MPD) thrusters have demonstrated performance levels and power handling capabilities of interest for Earth orbit, robotic planetary, cargo, and piloted missions. For MPD thrusters to successfully compete with conventional chemical propulsion systems, the thrusters will require power-to-thrust conversion efficiencies over 40% at specific impulses between 2500 – 5000 s. Near-term orbit-raising missions will require powers between 10 – 50 kW, whereas robotic and piloted planetary missions will

require powers between 50 kW and 1 MW. The required total impulses for Earth orbit, lunar, and Mars missions range from $1 \times 10^6$ to $1 \times 10^9$ N-s. To date, MPD thrusters have been operated continuously at powers over 500 kW at ~20% efficiency and 1500-s $I_{sp}$, or in a quasi-steady-state mode (with durations ~1 ms) at powers of several megawatts with efficiencies up to 40% and 5000-s $I_{sp}$.[1,2] The maximum demonstrated total impulse is $1 \times 10^6$ N-s. These thrusters have been tested with and without externally applied magnetic fields, and the applied-field thrusters have consistently shown better performance than those that rely solely on the self-induced magnetic field. While several authors have made this observation,[3,4] there is currently neither a fundamental understanding of applied-field MPD thruster performance nor a systematic data base from which to derive empirical scaling laws. Furthermore, it is critical that such a data base be established for numerical model verification. The purpose of this work was to address this lack by testing several thruster geometries in a systematic fashion over a wide range of operating conditions.

A typical MPD thruster, shown in Fig. 1, consists of a central cathode with a coaxial annular anode. Propellant, injected through an insulating boron nitride plate at the rear of the chamber, is heated, ionized, and accelerated via the in-
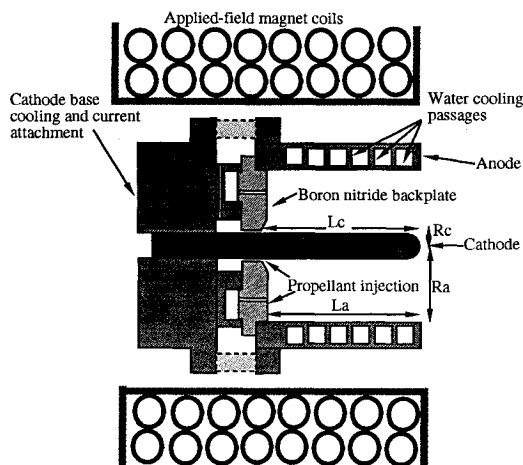
Fig. 1 MPD thruster schematic. Electrode dimensions are given in Table 1 (not to scale).

teraction of the discharge current and either the self-induced or externally applied magnetic field. The thruster power balance is usually dominated by the thrust power, unrecovered power used to heat and ionize the propellant, and the power deposited into the anode, with cathode power and radiation losses representing smaller fractions of the input power. The discharge voltage is determined by the ohmic dissipation, back emf, and the electrode fall voltages, where the latter play a dominant role in establishing the power deposited into the electrodes. Self-field thrusters must operate at very high current levels (over 10 kA) for the ohmic and back emf terms to dominate the electrode falls and, thus, enable deposition of most of the power into the accelerating plasma. For self-field thrusters operated at lower currents the electrode falls dominate the discharge voltage,[5] so that most of the discharge power is deposited into the electrodes. Applied-field thrusters mitigate this problem via an increased back emf, resulting in an increased discharge voltage. However, by itself this is insufficient to improve the thruster performance, since the additional energy deposited into the plasma must be converted into thrust power. Experimental studies have shown that both these phenomena, increased discharge voltage and enhanced thrust, occur with most applied-field thrusters. However, it is not possible from the available data to determine performance limits for these thrusters or establish what geometries and operating conditions are associated with improved performance. Correlations between the life-limiting mechanisms and performance have not been addressed at all.

This article presents the results of performance measurements made on eight MPD thruster geometries operated using argon propellant at power levels between 20–130 kW. While hydrogen has been shown to yield superior performance,[6] facility limitations precluded its use for a wide range of thruster geometries. The thruster geometries were chosen so as to permit, as far as possible, isolation of the effects of the individual parameters. Following a discussion of the thruster designs and experimental facility, the results of the performance and power balance measurements are presented. The implications of these results for applied-field MPD thruster scaling are then discussed in the context of existing theoretical models for these thrusters. Finally, a summary of the major conclusions from this work is presented.

## Experimental Apparatus

### Thruster and Applied Field Magnet Designs

The thrusters, shown schematically in Fig. 1, consisted of a water-cooled cylindrical copper anode with a coaxial, 2% thoriated tungsten cathode. The cathode was cooled by conduction to a water-cooled copper clamp. A boron nitride backplate was used to inject propellant through holes located near the midradius between the anode and cathode, and through an annulus at the cathode base. The dimensions of the electrode geometries tested are given in Table 1. The cathode used for geometry G had a conical tip, all other cathode tips were hemispherical. In addition to the cylindrical anodes (geometries A – G), a 7.6-cm-long flared anode was tested. The flared anode (geometry H) had a 2.5-cm upstream radius and a 5.1-cm-radius exit plane with an expansion angle of 33 deg.

The flared anode thruster dimensions were chosen to permit direct comparison with the 2.5- and 5.1-cm-radius straight cylinder anodes.

The MPD thrusters were mounted inside solenoidal coils used to generate the applied magnetic fields. Two 15.3-cm-long applied-field magnets, with bore diameters of 15.3 and 20.3 cm, were required to accommodate the anodes and maximize the potential applied field strength.[7] The 15.3-cm-diam magnet was used for tests of geometries A, B, and G, and the 20.3-cm-diam magnet was used for geometries C – F and H. All thrusters were mounted such that the anode exit plane was flush with the end of the solenoid. The axial field strengths were measured as a function of magnet current and checked for symmetry. These calibrations yielded axial field strengths of $1.66 \times 10^{-4}$ T/A and $8.48 \times 10^{-5}$ T/A at the centerline of the magnet exit plane for the 15.3 and 20.3 cm magnets, respectively. All reported field strengths were measured at the centerline of the magnet exit plane.

### Vacuum Facility, Power, and Propellant Management Systems

The MPD thruster test stand was mounted inside a 3-m-diam test chamber separated from the main 7.6-m-diam, 21-m-long tank by a 3-m-diam gate valve.[7] The main tank was pumped by 20 0.9-m-diam oil diffusion pumps backed by three roots blowers and two roughing pumps. This facility maintained a back pressure below 0.07 Pa at argon flow rates below 0.16 g/s. This pressure is adequate to ensure negligible background gas entrainment.[8]

The thruster power supply consisted of a series-parallel network of six 65-kW arc-welding supplies. This network, which supplied up to 3000 A at 130 V, was electrically isolated from ground. A single 65-kW welding supply provided up to 1500 A to the applied-field magnet. The thruster was ignited using a 2-kW 900-V supply attached to the thruster electrodes in parallel with the main power system. The welding supply ripple magnitude varied from 20 to 30%, depending on thruster geometry and operating condition.[7]

Propellant flow rates were measured using thermal conductivity-type flow controllers with 2% precision. A constant-volume calibration system showed that the propellant flow rate was accurate to within 3%.

### Performance and Power Balance Measurements

Measurements of thrust, discharge current and voltage, and propellant flow rate were required to establish thrust efficiency and specific impulse, defined by

$$\eta = (T^2/2\dot{m}V_dJ_d) \qquad I_{sp} = (T/\dot{m}g_0) \qquad (1)$$

No effort was made to subtract cold-flow thrust or to include the applied-field magnet power in the calculations. The latter was justified on the basis that the magnet power can be reduced to a negligible fraction of the thruster power via a simple redesign of the coils.[9] The thrust stand consisted of an inverted pendulum with a oscillation damping circuit, remote leveling apparatus, and an in situ calibration mechanism.[10] The leveling mechanism compensated for tank distortions during pumpdown and for the different masses and c.g. of the various thruster configurations. The influence of the applied-field

**Table 1  Dimensions of the MPD thrusters tested**

| Geometry | Anode radius, cm | Anode length, cm | Cathode radius, cm | Cathode length, cm |
|---|---|---|---|---|
| A | 2.5 | 7.6 | 0.64 | 7.6 |
| B | 3.81 | 7.6 | 0.64 | 7.6 |
| C | 5.1 | 7.6 | 0.64 | 7.6 |
| D | 5.1 | 15.2 | 0.64 | 7.6 |
| E | 5.1 | 7.6 | 1.27 | 7.6 |
| F | 5.1 | 15.2 | 1.27 | 7.6 |
| G | 3.81 | 7.6 | 0.64 | 2.5 |
| H | 2.5–5.1 (flared) | 7.6 | 0.64 | 7.6 |

magnet on the thrust measurement was checked before and after each test. In addition, tests were performed to quantify the influence of the discharge current and thrust stand heating on the thrust measurement, including one in which the cooling water temperature was raised to over 66°C to simulate the effects of high-power thruster operation on the current conducting flexures. These tares never exceeded 0.01 N, or approximately 1% of the typical thrust levels. However, extended (>2 h) thruster operation at powers over 100 kW could introduce zero shifts of up to 0.1 N. Periodic repetition of the initial operating point during extended tests kept the thrust error below 3%.

The anode heat transfer and the heat conducted into the cathode base were measured calorimetrically by monitoring the cooling water temperature rise and flow rate. The flow rate was determined using turbine flow meters accurate to 2%. The temperatures were measured to within ±0.2°C, and the water flow rate was adjusted so that the temperature rise was over 10°C.

As discussed below, anode power deposition was by far the dominant loss for all operating conditions. For argon propellant the convective and radiative terms of the anode power balance are small, leading to the power deposition equation[11]:

$$P_a = J_e[V_a + (5kT_e/2e) + \phi_e]  \qquad (2)$$

The first term in Eq. (2) represents the contribution of the anode fall voltage, the second term represents the thermal energy of the incoming electrons, and the third term represents the contribution of the anode work function. The fall voltage in this context is not the sheath voltage, but rather represents the directed energy of the electrons when they hit the anode. The electron temperature inside the chamber was not measured, and so the effects of the anode fall could not be isolated. However, Gallimore[12] showed that when using argon propellant the dominant contribution to the anode power came from the anode fall voltage, and that the relative contributions of the terms did not change dramatically with increasing applied field strength. In this work the "effective anode fall voltage" was calculated by dividing the anode power by the discharge current.

## Thruster Performance and Power Balance

Each test began by presetting the mass flow rate and allowing the tank background pressure to stabilize. The applied-field magnet was then turned on; countdown timers activated the main power supply, injected a high-pressure gas pulse (if necessary for ignition), and turned on the high-voltage igniter in a preset sequence. The ignition phase was usually characterized by some particulate ejection that ended within 1 – 3 s if the thruster was operating properly. The thruster was kept at a given operating point for a few minutes before a data set was taken, and each measurement was taken several times and over several tests to ensure repeatability. An attempt was made to determine the stable operating envelope for each thruster geometry, although this was precluded in several cases by the limited cooling capacity of the water heat exchangers. Turning the applied magnetic field off always resulted in unstable operation characterized by particulate emission.[7,8]

All data shown were taken with an argon flow rate of 0.1 g/s at a discharge current of 1000 A. Weight loss measurements of the cathode, anode, and boron nitride backplate showed that their mass loss rates never exceeded 0.5% of the propellant flow.[13]

### Influence of Anode Radius

Changing the anode radius and shape had large effects on the terminal voltage, $I_{sp}$, and efficiency, as shown in Figs. 2 – 4. Geometries A – C, and H were used for these tests. The large scatter in the terminal voltage observed at low applied
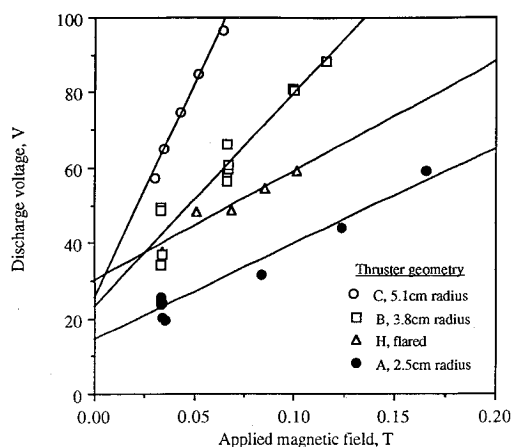


Fig. 2   Influence of anode radius on discharge voltage. $L_a = 7.6$ cm, $J_d = 1000$ A, 0.1 g/s argon.
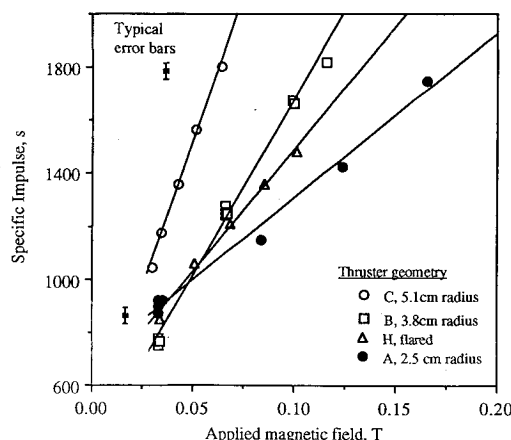


Fig. 3   Effect of anode radius on the specific impulse. $L_a = 7.6$ cm, $J_d = 1000$ A, 0.1 g/s argon.
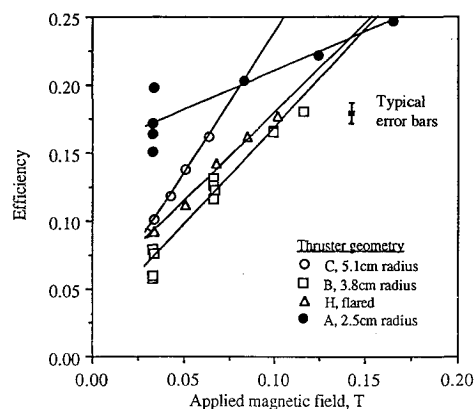


Fig. 4   Effect of anode radius on thruster efficiency. $L_a = 7.6$ cm, $J_d = 1000$ A, 0.1 g/s argon.

magnetic field strengths with geometry B was due to changes in the anode power deposition (see below). The discharge voltage, $I_{sp}$, and efficiency increased nearly linearly with applied-field strength, up to maxima limited by the thruster water cooling capacity. The highest efficiency for these operating conditions was 23%, measured with the smallest radius cylindrical anode (geometry A). The highest measured $I_{sp}$ for these geometries and operating conditions was 1800 s. Listed in Table 2 are the slopes of the linear least-squares fits to the data. The rate of increase with applied-field strength of all three performance parameters increased approximately quadratically with anode radius for the cylindrical thrusters. The flared anode thruster (geometry H) slopes were close to those of the 2.5-cm-radius anode (geometry A) for the voltage and

Table 2  Least-squares slopes for discharge voltage, $I_{sp}$, and efficiency vs applied field strength
for four anode geometries

| Geometry | $V_d$ vs $B_z$ slope, V/T | $I_{sp}$ vs $B_z$ slope, s/T | $\eta$ vs $B_z$ slope, $T^{-1}$ | $\eta$ vs $I_{sp}$ slope, $s^{-1}$ |
|----------|----------|----------|----------|----------|
| A | 254 | 6,171 | 0.60 | $9.76 \times 10^{-5}$ |
| B | 569 | 13,275 | 1.43 | $1.08 \times 10^{-4}$ |
| C | 1,141 | 22,120 | 2.07 | $9.35 \times 10^{-5}$ |
| H | 291 | 9,185 | 1.30 | $1.41 \times 10^{-4}$ |
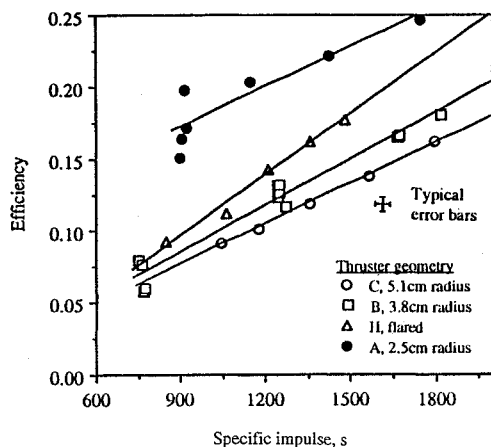


Fig. 5  Efficiency vs specific impulse for four anode radii. $L_a$ = 7.6 cm, $J_d$ = 1000 A, 0.1 g/s argon.
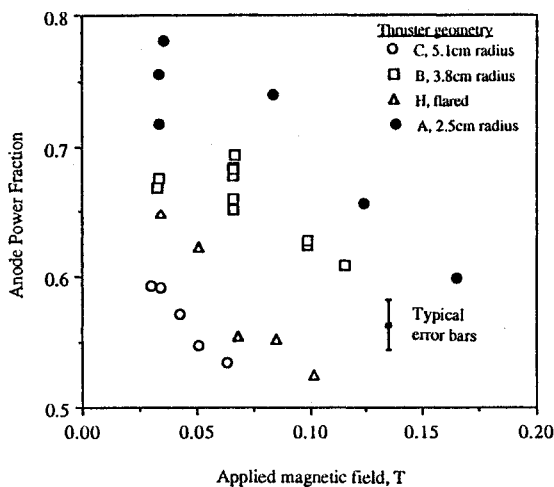


Fig. 6  Effect of anode radius on anode power fraction for four anode radii. $L_a$ = 7.6 cm, $J_d$ = 1000 A, 0.1 g/s argon.
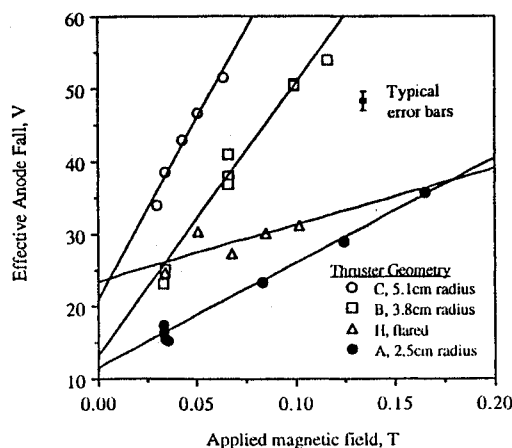


Fig. 7  Effect of anode radius on the effective anode fall voltage. $L_a$ = 7.6 cm, $J_d$ = 1000 A, 0.1 g/s argon.
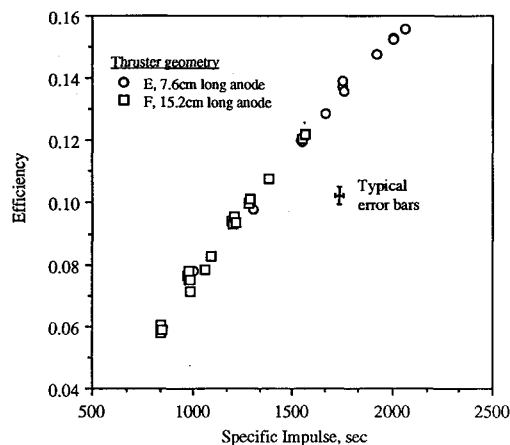


Fig. 8  Efficiency vs specific impulse for two anode lengths. $R_a$ = 5.1 cm, $J_d$ = 1000 A, 0.1 g/s argon.

between those for geometry A and B for the $I_{sp}$. The rate of efficiency increase (Table 2) for the flared anode thruster was close to that of geometry B. These differences are reflected in the $\eta - I_{sp}$ characteristics, shown in Fig. 5, where the flared anode thruster has the highest slope and the three cylindrical geometries all have similar, although lower, slopes.

The effects of applied-field strength and anode radius on anode power deposition and the effective anode fall are shown in Figs. 6 and 7. The anode power fraction decreased with both increasing applied-field strength and anode radius. The anode power fraction of the flared anode geometry was closest to that of the largest cylindrical thruster, geometry C, and fell more rapidly with increasing applied-field strength than that for the cylindrical thrusters. This is reflected in the behavior of the effective anode fall voltage (Fig. 8) which increased linearly with the applied-field strength for all geometries. The large scatter for geometry B was directly reflected in the discharge voltage, but did not influence the thrust. The effective anode fall for the flared anode thruster had the lowest dependence on the applied-field strength.

For the operating conditions tested, the efficiency was highest with the smallest-radius thruster (Fig. 5), whereas the anode power fraction was smallest with the largest radius thruster (Fig. 6). This shows that the efficiency with which power deposited into the plasma was converted to thrust was significantly higher with the smaller thruster.

### Influence of Anode Length

The effect of anode length was tested with the 5.1-cm-radius cylindrical anode using lengths of 7.6 and 15.2 cm (geometries E and F). Doubling the anode length reduced the discharge voltage, $I_{sp}$, and efficiency, by approximately 17 V, 350 s, and 2.5 absolute percentage points, respectively, but did not significantly affect the rate of change of these parameters with the magnetic field. The changes are much larger than the measurement errors. The maximum $I_{sp}$ and $\eta$ obtained with the long anode thruster were 1500 s and 12%, respectively. The impact of these changes on the $\eta - I_{sp}$ characteristic are shown in Fig. 8. While the two geometries lie on the same overall curve, data taken with the longer anode appear only in the lower ranges of $\eta$ and $I_{sp}$. Thus, anode length does not have the same fundamental influence as the anode radius,
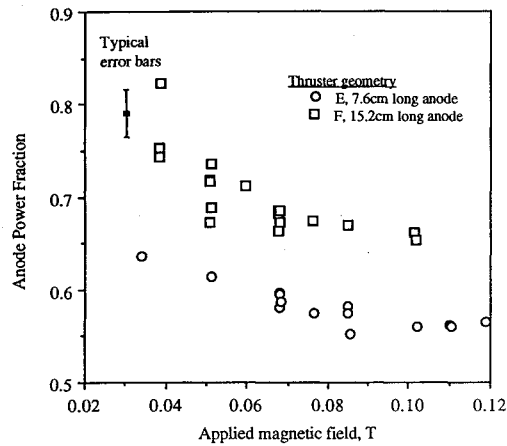
Fig. 9  Effect of anode length on anode power fraction. $R_a$ = 5.1 cm, $J_d$ = 1000 A, 0.1 g/s argon.
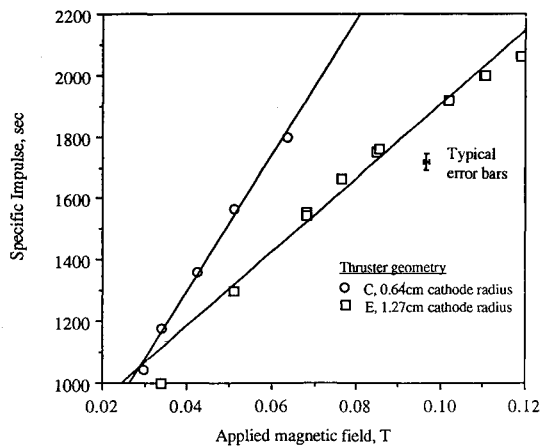


Fig. 10  Effect of cathode radius on specific impulse. $R_a$ = 5.1 cm, $J_d$ = 1000 A, 0.1 g/s argon.
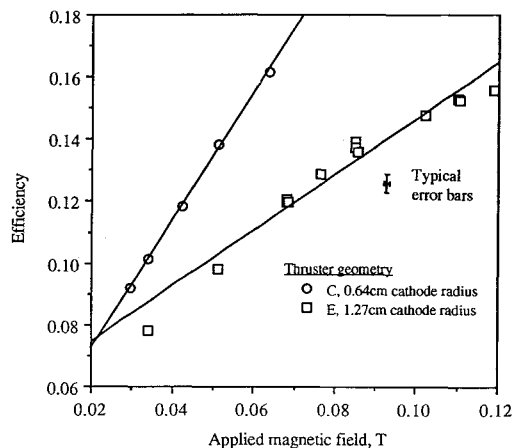


Fig. 11  Effect of cathode radius on thruster efficiency. $R_a$ = 5.1 cm, $J_d$ = 1000 A, 0.1 g/s argon.

although it does affect the applied-field strength required to achieve a given performance level.

Figure 9 shows the effect of anode length and applied-field strength on the anode power fraction. The anode power fraction for the longer anode was about 10% higher than that for the shorter anode, reaching a minimum value of ~67% at the highest applied-field strength tested. However, the effective fall voltage for the long anode was actually about 7 V lower than that with the short anode, although the rate at which the effective fall voltage increased with the applied-field was the same for both geometries. The highest measured effective fall voltage with the long anode was 60 V at a field strength

of 0.10 T. The observed increase in anode power fraction resulted from the proportionally larger drop in the terminal voltage. While the cause of the terminal voltage drop is not known, the increased anode power fraction caused the decrease in thruster efficiency.

### Influence of Cathode Radius

Doubling the cathode radius had little effect on the discharge voltage magnitude, and only a slight effect on its rate of increase with magnetic field, with $V_d$ increasing slightly more rapidly with the smaller radius anode. This behavior was also observed at other discharge currents. The discharge voltage increased from ~55 V at 0.03 T with both cathode geometries to ~98 and ~130 V with the small and large radius cathodes, respectively, at the highest field strengths achieved. The maximum applied-field strength with the 0.64-cm-radius cathode, geometry C, was reached at a field strength of 0.065 T, when sparks were observed coming out of the chamber. No such phenomena were observed with the larger cathode, for which the maxima was due to the magnet power supply. Video imaging of the chamber interior during thruster operation revealed that increasing the applied-field strength resulted in the formation of a high-temperature zone at the cathode base, and the sparks observed with the small cathode resulted from local melting of the cathode at the base. The power density reduction resulting from use of the large radius cathode prevented the local melting. As shown in Figs. 10 and 11, the cathode radius had a large effect on the $I_{sp}$ and efficiency, with the 0.64-cm-radius cathode yielding higher specific impulses and correspondingly higher efficiencies. The slope of the least-squares fit to both parameters is inversely proportional to the cathode radius. The $\eta - I_{sp}$ characteristic (Fig. 12) shows that use of the smaller radius cathode resulted in a higher magnitude and slope than the larger cathode.

The anode power fraction, shown as a function of applied-field strength in Fig. 13, was ~10% lower for the small radius cathode. However, the effective anode fall voltage was the same for these two geometries, increasing from ~35 V at an applied field strength of 0.033 T to ~73 V at 0.12 T. Thus, the difference in power fraction was due solely to a small increase in the voltage across the plasma.

### Influence of Cathode Length

The short cathode used for this study, geometry G, had a conical tip and was 2.5 cm long. Cathode length had no effect on the discharge voltage, which increased from ~40 V at low applied-field strength to ~115 V at the higher field strengths for both long and short cathodes. However, both the $I_{sp}$ and efficiency, shown in Figs. 14 and 15, were higher with the short cathode thruster, although their rate of increase with magnetic field strength was lower than that with the long cathode thruster. The maximum $I_{sp}$ and efficiency, 2300 s at 23%, were measured with the short cathode thruster. Changing the cathode length did not affect the shape of the $\eta - I_{sp}$ characteristic (Fig. 16), although the long cathode data was restricted to the lower ranges of efficiency and $I_{sp}$. This effect is similar to that of the anode length.

Reducing the cathode length reduced the anode power fraction by ~25%. Figure 17 shows that while the anode power fraction decreased rapidly from about 72 to 60% for the long cathode, it never exceeded 52% for the short cathode. While there is substantial scatter in the effective anode fall at low applied-fields, the rate of increase of the effective anode fall voltage was the same for both cathode geometries, although its magnitude was approximately 6 V higher with the long cathode. In contrast to the case with the anode length, the difference in thrust efficiencies for the two cathode lengths cannot be explained solely on the basis of changes in the anode power fraction. For example, at a field strength of 0.12 T, the anode power fraction was 25% less with the short cathode thruster, but the thrust efficiency was only ~10% higher.
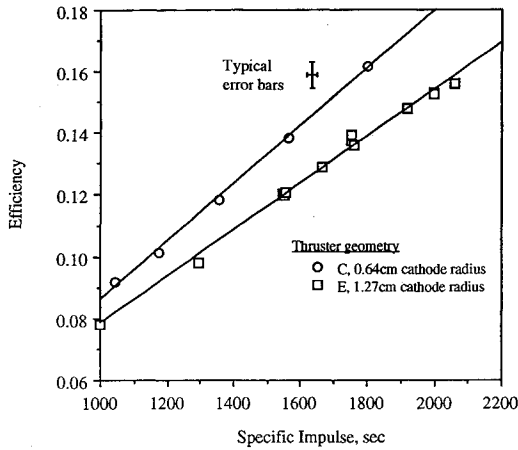
Fig. 12   Efficiency vs specific impulse for two cathode radii. $R_a = 5.1$ cm, $J_d = 1000$ A, 0.1 g/s argon.
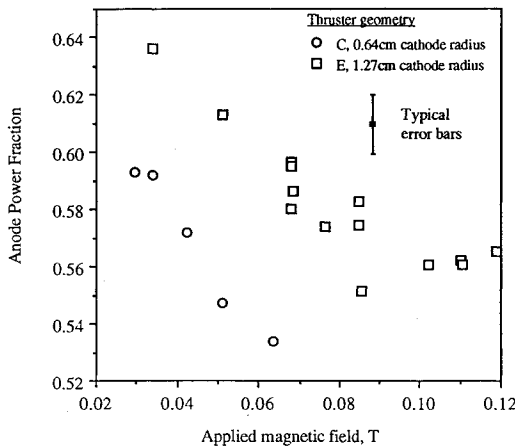
Fig. 13   Effect of cathode radius on anode power fraction. $R_a = 5.1$ cm, $J_d = 1000$ A, 0.1 g/s argon.
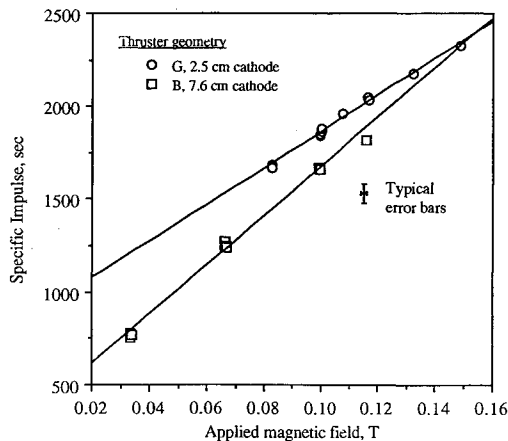
Fig. 14   Effect of cathode length on the specific impulse. $R_a = 3.8$ cm, $J_d = 1000$ A, 0.1 g/s argon.

Fig. 15   Effect of cathode length on thruster efficiency. $R_a = 3.8$ cm, $J_d = 1000$ A, 0.1 g/s argon.

Fig. 16   Efficiency vs specific impulse for two cathode lengths. $R_a = 3.8$ cm, $J_d = 1000$ A, 0.1 g/s argon.

Fig. 17   Effect of cathode length on anode power fraction. $R_a = 3.8$ cm, $J_d = 1000$ A, 0.1 g/s argon.

Other loss mechanisms must have increased when the cathode length was decreased.

Decreasing the cathode length had the same effect on the effective anode fall as increasing the anode length, with both changes resulting in a ~7-V reduction. However, only the cathode change resulted in a performance improvement, because increasing the anode length decreased the discharge voltage to the point that the anode power fraction increased. Shortening the cathode had a dramatic effect on the plume characteristics,[4] an effect that was not observed when the anode length was increased. These observations may be the result of the combined effects of shortening the cathode and
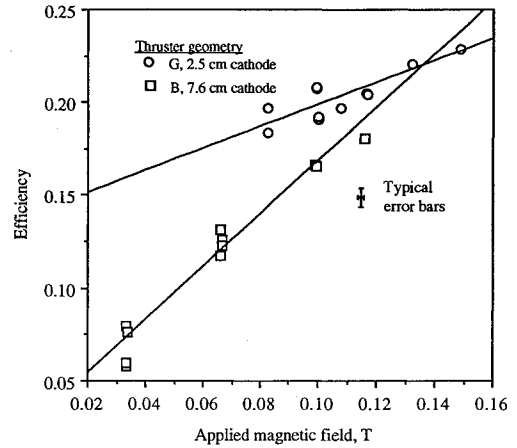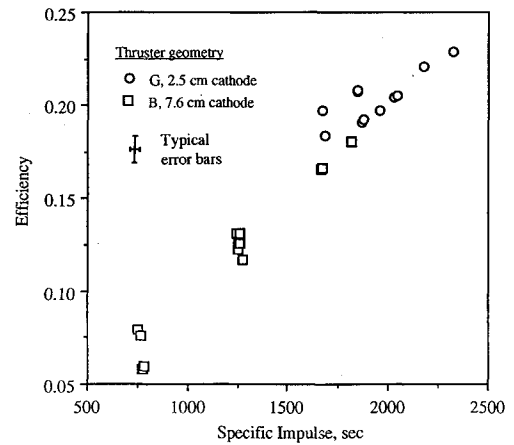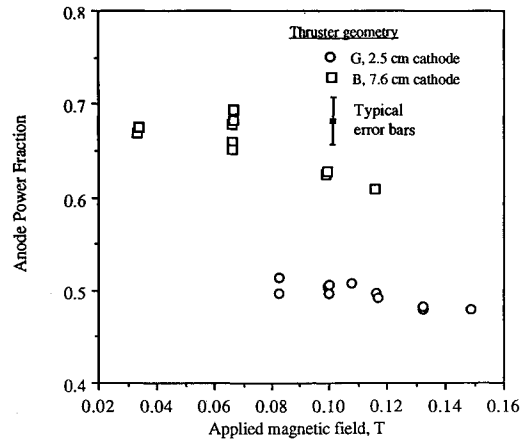
changing the tip shape to a cone, which would both increase current emission from the tip and improve the flowfield around it.[4]

## Scaling Relationships

The above data were used to establish the dependencies of the thruster performance parameters on thruster geometry. Partial derivatives of discharge voltage and $I_{sp}$ with respect to applied-field strength were obtained from the data to extract the functional forms of these relationships. The result for $I_{sp}$ was

$$I_{sp} = (R_a^2/k_1 L_c R_c)B_z + k_2 f(L_a^{-1})  \qquad (3)$$

where the second term indicates that while the thrust decreased with increasing anode length, the length had no effect on the influence of the magnetic field. For the discharge voltage the result was

$$V_d = (R_a^2/k_3 R_c)B_z + k_4 f(L_a^{-1}) \qquad (4)$$

where again, the second term represents the reduction in discharge voltage with anode length.

The only known analytic model for applied-field MPD thruster plasma acceleration is that of Fradkin.[14] In that work, relations were derived for the thrust and plasma potential drop as functions of applied-field strength and thruster geometry by assuming that the plasma acceleration resulted from the recovery of azimuthal momentum imparted to the flow by the azimuthal Lorentz force resulting from the radial discharge current interacting with the axial applied magnetic field. The azimuthal momentum was assumed to be converted to axial momentum with unit efficiency during the plasma expansion in the diverging applied magnetic field. The plasma was also assumed to rotate as a solid body. Contributions due to the self-induced magnetic field, pressure forces, and azimuthal currents interacting with the radial magnetic field and electrode falls were neglected. Neglect of self-field terms was easily justified for the discharge current of 1000 A and 0.1 g/s flow rate used in this work. The self-field $I_{sp}$ should be close to[15]

$$I_{sp,sf} = (\mu_0 J_d^2/4\pi \dot{m} g_0)[\ell_n(R_a/Rc) + \tfrac{1}{2}] \qquad (5)$$

which depends only on the discharge current and the anode to cathode radius ratio. The self-field $I_{sp}$ for the conditions in these tests were 193, 233, and 263 s for the 2.5-, 3.81-, and 5.1-cm anode radius thrusters, respectively, with the 0.69-cm cathodes. These values are far below the measured values, which increased from ~800 to ~1800 s with increasing applied-field strength. This clearly shows that the dominant propellant acceleration in the MPD thrusters tested in this work resulted from the applied magnetic field. Neglect of thermal acceleration and azimuthal current terms relied on assumed plasma properties (ion temperature and density gradients) for which there was little supporting data. Neglect of the electrode falls hampers comparisons with experiment results unless there was a way to account for them, but this was not possible in this study due to the absence of electron temperature measurements close to the anode. The model results were

$$I_{sp} = (1/\sqrt{2})(B_z J_d R_a/\dot{m} g_0)[1 - \tfrac{3}{2}(R_c/R_a)^2] \qquad (6)$$

$$V_d = V_c + (B_z^2 J_d R_a^2/2\dot{m}) \qquad (7)$$

where $V_c$ is the voltage drop due to ohmic heating and the electrode falls. The model correctly predicted the linear dependence of $I_{sp}$ on magnetic field strength, and the quadratic increase in $V_d$ with anode radius. However, for the conditions studied in this work the $I_{sp}$ increased quadratically, not linearly, with anode radius, and the $V_d$ increased linearly, not quadratically, with applied-field strength. In addition, the model dependence on cathode radius is very weak, in contrast to the experimental results. While the measured effect of anode length may be a result of viscous effects, which were neglected in the model, the cathode length plays a different role since it affected both the magnitude and the rate of thrust increase with applied-field. It is not clear which of the model assumptions break down for the operating conditions used in this work.

The effective anode fall voltage increased linearly with applied-field strength for all geometries. The only geometric parameters that altered the slope of the effective fall voltage vs applied-field strength were the anode radius and shape, although it was not possible to establish a quantitative dependence. The effective fall voltage decreased slightly with

increasing anode length and with decreasing cathode length. It was independent of cathode radius.

The dependence of the effective electrode fall voltage on the applied magnetic field indicates that the sheath was magnetized.[16] This occurs whenever the electron cyclotron radius is comparable to or smaller than the Debye length and the electron Hall parameter is greater than one. These quantities were calculated from[17]

$$\frac{r_c}{\lambda_D} = \frac{7.5 \times 10^{-11}}{eB_z}\sqrt{m_e n_e} \qquad (8)$$

$$\frac{\omega_{ce}}{\nu_{e\text{-}i}} = \frac{eB_z T_e^{1.5}}{2 \times 10^{-6} m_e n_e \, \ell_n(\Lambda)} \qquad (9)$$

where the coulomb logarithm and the ion charge were given constant values of 10 and 1 (singly ionized), respectively, and so the results should be within a factor of 2 of actual values. Electron densities and temperatures were chosen that bracket measurements made using electrostatic probes close to the thruster exhaust plane.[7,18] For the operating conditions studied, $r_i/\lambda_D$ ranged from 0.4 to over 10, and the electron Hall parameter ranged from ~80 to over 1000. These estimates substantiate the conclusion that the magnetic field impedes electron motion in the anode fall region, and show that electrode models for applied-field thrusters must include magnetic field effects. Similar effects have been observed in fundamental electrode studies using free-burning arcs with applied magnetic fields[19] and in self-field thrusters,[20] although in the latter case it was found that the magnitude of the electron Hall parameter was too small to explain the measurements.

The linear rise in effective anode fall voltage with applied-field strength can be explained in part by considering the flux of electrons into the anode, given by[21]

$$\Gamma_e = -D_e \frac{dn_e}{dy} - \mu_e n_e E \qquad (10)$$

Using the Bohm diffusion coefficient[17] for $D_e$ and rearranging using Einstein's relation between the diffusion coefficient and the electron mobility, yields

$$E = -\frac{1}{en_e}\left(16 j_e B_z + kT \frac{dn_e}{dy}\right) \qquad (11)$$

which shows that, to a first order, the electric field required to maintain a constant electron current increases linearly with magnetic field strength. Note that classical diffusion predicts a quadratic increase in electric field with magnetic field strength, a dependence that is clearly not observed in these measurements. In addition, the decrease in plasma density associated with larger thruster sizes may be the cause of the observed anode radius dependence. A decrease in plasma density results in an increased electron Hall parameter and decreases the rate of cross-field diffusion to the anode, requiring a higher electric field at the anode to conduct the discharge current. Lower effective fall voltages observed with hydrogen support this argument,[8] since the greater number densities associated with hydrogen at a given flow rate would reduce the Hall parameter. The observed slow increase of the effective fall voltage with applied-field strength with the flared anode thruster is likely due to the intersection of the anode surface with the magnetic field lines. This would permit current carrying electrons to travel along field lines into the anode, reducing the requirement for cross-field conduction.

These results indicate three clear directions for changing the thruster geometry to improve thruster performance. First, the observed rapid increase in thruster performance with applied-field strength when using the larger anode radii indicate that both larger anodes and increased magnetic fields should

be tested. Second, using a recessed cathode with a short anode yielded the highest measured performance due to the reduction of anode losses. Third, designing the anode and applied-field so that the field lines cross the anode surface, thus reducing the requirement for a high anode fall voltage, should also reduce the anode power loss and increase thruster efficiency. Although the flared-anode appears to have achieved this effect, use of a converging or a converging-diverging anode design should be explored.

## Conclusions

Eight applied-field MPD thruster geometries were tested with argon propellant at a discharge current of 1000 A to establish the dependence of thruster performance on geometric scale and applied field strength. Anode and cathode radii and lengths were varied over a factor of 2 for a range of operating conditions. Efficiency and specific impulse were found to increase approximately linearly with applied-field strength, achieving values over 10 times those expected for purely self-field acceleration. A peak performance of 2300 s $I_{sp}$ at 23% efficiency was measured with a 7.6-cm-long, 7.6-cm-diam anode, with a 2.5-cm-long, 1.2-cm-diam cathode thruster at a power level of 113 kW. The largest thruster power sink was the anode, which consumed between 50–80% of the input power. Both thrust and discharge voltage increased linearly with applied-field strength, quadratically with anode radius, and decreased with increasing cathode radius. The thrust decreased with increasing cathode and anode length, although the latter did not affect the thrust vs applied-magnetic field slope. The voltage was independent of cathode length, and it was higher with a shorter anode. These results showed that only the electrode radii have a fundamental impact on the efficiency-specific impulse characteristic, with smaller radius electrodes having higher efficiencies at a given specific impulse for the operating conditions studied. The observed scaling with electrode radii for applied-field thrusters was very different than that for self-field thrusters, for which thrust scales as $ln(R_a/R_c)$. The electrode lengths merely changed the required applied-field strength to achieve the desired performance. The effective anode fall behavior shows that the sheath is magnetized, and indicates that the anode power would be reduced if the magnetic field were shaped to cross the anode surface.

## Acknowledgments

## References

[1]Sovey, J., and Mantenieks, M. A., "Performance and Lifetime Assessment of MPD Arc Thruster Technology," *Journal of Propul-*

*sion and Power*, Vol. 7, No. 1, 1991, pp. 71–83.

[2]Myers, R. M., Mantenieks, M. A., and LaPointe, M. R., "MPD Thruster Technology," AIAA Paper 91-3568, Sept. 1991; see also NASA TM 105242, Sept. 1991.

[3]Tahara, H., Yasui, H., Kagaya, Y., and Yoshikawa, T., "Development of a Quasi-Steady MPD Arcjet Thruster for Near-Earth Missions," AIAA Paper 87-1001, May 1987.

[4]Kagaya, Y., Yoshikawa, T., and Tahara, H., "Quasi-Steady MPD Arcjets with Applied Magnetic Fields," AIAA Paper 85-2001, Oct. 1985.

[5]Myers, R. M., Kelly, A. J., and Jahn, R. G., "Energy Deposition in Low-Power Coaxial Plasma Thrusters," *Journal of Propulsion and Power*, Vol. 7, No. 5, 1991, pp. 732–739.

[6]Myers, R. M., "Applied-Field MPD Thruster Performance with Hydrogen and Argon Propellants," *Journal of Propulsion and Power*, Vol. 9, No. 5, 1993, pp. 781–784.

[7]Myers, R. M., Wehrle, D., Vernyi, M., Biaglow, J., and Reese, S., "A Preliminary Characterization of Applied Field MPD Thruster Plumes," AIAA Paper 91-2339, June 1991; see also NASA CR 187165.

[8]Myers, R. M., "Applied Field MPD Thrusters Geometry Effects," AIAA Paper 91-2339, June 1991; see also NASA CR 187163.

[9]Myers, R. M., Parkes, J. E., and Mantenieks, M. A., "Multi-megawatt MPD Thruster Design Consideration," *9th Symposium on Space Nuclear Power Systems*, 1992, pp. 1279–1286 (AIP CP 246).

[10]Haag, T., "Thrust Stand for High Power Electric Propulsion Devices," *Review of Scientific Instruments*, Vol. 62, No. 5, 1991, pp. 1186–1191.

[11]Saber, A. J., and Jahn, R. G., "Anode Power Deposition in Quasi-Steady MPD Arcs," AIAA Paper 73-1091, Oct. 1973.

[12]Gallimore, A. D., Myers, R. M., Kelly, A. J., and Jahn, R. G., "Anode Power Deposition in an Applied-Field Segmented Anode MPD Thruster," *Journal of Propulsion and Power*, Vol. 10, No. 2, 1994, pp. 262–268.

[13]Mantenieks, M. A., and Myers, R. M., "Component Erosion in 100-kW Class Applied-Field, Water-Cooled MPD Thrusters," 23rd Intern. Electric Propulsion Conf., IEPC 93-121, Seattle, WA, Sept. 1993.

[14]Fradkin, D. B., Blackstock, A. W., Roehling, D. J., Stratton, T., Williams, M., and Lieweter, K. W., "Experiments Using a 25-kW Hollow Cathode Lithium Vapor MPD Arcjet," *AIAA Journal*, Vol. 8, No. 5, 1970, pp. 886–894.

[15]Gilland, J., "Influence of Geometric Scale upon MPD Thruster Performance," M.S. Thesis, Princeton Univ., Princeton, NJ, March 1988.

[16]Myers, R. M., Mantenieks, M., and Sovey, J., "Geometric Effects in Applied-Field MPD Thrusters," AIAA Paper 90-2669, July 1990; see also NASA TM 103259, July 1990.

[17]Chen, F., *Introduction to Plasma Physics and Controlled Fusion*, Vol. 1, Plenum Press, New York, 1985.

[18]Myers, R. M., "Plume Characteristics of MPD Thruster: A Preliminary Examination," AIAA Paper 89-2832, July 1989; see also NASA CR 185130, Sept. 1989.

[19]Soulas, G. C., and Myers, R. M., "Mechanisms of Anode Power Deposition in a Low Pressure Free-Burning Arc," 23rd Intern. Electric Propulsion Conf., IEPC-93-194, Seattle, WA, Sept. 1993.

[20]Gallimore, A. D., Kelly, A. J., and Jahn, R. G., "Anode Power Deposition in Magnetoplasmadynamic Thruster," *Journal of Propulsion and Power*, Vol. 9, No. 3, 1993, pp. 361–368.

[21]Kalikhman, L., *Elements of Magnetogasdynamics*, translated by Scripta Technica, Inc., W. B. Saunders, Philadelphia, PA, 1967.